

TIC 184743498: The First Tri-Axial Stellar Pulsator

Valencia Zhang^{1*}, Saul Rappaport², Rahul Jayaraman², Donald W. Kurtz^{3,4},
Gerald Handler⁵, James Fuller⁶, and Tamas Borkovits^{7,8,9,10,11}

¹Phillips Academy, Andover, MA, 01810, USA

²Department of Physics, and Kavli Institute for Astrophysics and Space Research, M.I.T., Cambridge, MA 02139, USA

³Centre for Space Research, North-West University, Mahikeng 2745, South Africa

⁴Jeremiah Horrocks Institute, University of Central Lancashire, Preston PR1 2HE, UK

⁵Nicolaus Copernicus Astronomical Center, Polish Academy of Sciences, ul. Bartycka 18, 00-716, Warszawa, Poland

⁶TAPIR, Mailcode 350-17, California Institute of Technology, Pasadena, CA 91125, USA

⁷Baja Astronomical Observatory of University of Szeged, H-6500 Baja, Szegedi út, Kt. 766, Hungary

⁸HUN-REN-SZTE Stellar Astrophysics Research Group, H-6500 Baja, Szegedi út, Kt. 766, Hungary

⁹Konkoly Observatory, HU-REN Research Centre for Astronomy and Earth Sciences, H-1121 Budapest, Konkoly Thege Miklós út 15-17, Hungary

¹⁰ELTE Eötvös Loránd University, Gothard Astrophysical Observatory, Szent Imre h. u. 112, 9700 Szombathely, Hungary

¹¹HUN-REN-ELTE Exoplanet Research Group, H-9700 Szombathely, Szent Imre h. u. 112, Hungary

Accepted XXX. Received YYY; in original form ZZZ

ABSTRACT

We have discovered a δ Scuti pulsator in a tight binary ($P = 1.053$ d) with nine pulsation modes whose frequencies are between 38 and 56 d^{-1} . Each of these modes exhibits amplitude modulations and π -rad phase shifts twice per orbital cycle. Five of these modes exhibit amplitude and phase shifts that are readily explained by dipole pulsations along an axis that is aligned with the binary’s tidal axis. The novelty of the system lies in the remaining four pulsation modes, which we show are dipole pulsations along an axis that is perpendicular to both the tidal axis and the binary’s orbital angular momentum axis. There are additionally two pulsation modes whose amplitudes and phases do not change significantly with orbital phase; they are explained as dipole modes along an axis aligned with the orbital/rotation axis. Hence, we propose that TIC 184743498 is a tri-axial pulsator, the first of its kind.

Key words: stars: oscillations – stars: variables – stars: individual (TIC 184743498)

1 INTRODUCTION

Studies of the photometric variability of stars due to stellar pulsations have been carried out for over a century. For instance, the variability of the bright early F-type star, Delta Scuti (δ Sct), which lends its name to an entire class of pulsating stars, was discovered in radial velocities by Campbell & Wright (1900). They found a range of about 10 km s^{-1} in 7 measurements made from 1899 to 1900. Fath (1935) and Colacevich (1935) noted sinusoidal photometric variability in δ Sct stars with maximum light at minimum radial velocity over a period of 0.193 d, and concluded that the star is not a spectroscopic binary. Baglin et al. (1973), Breger (1979, 2000), and Kurtz (2022) summarize more recent work on this class of star.

δ Sct stars, along with almost all other classes of pulsating variables, are observed to have nonradial modes. Unlike the symmetrical radial pulsations of the dominant modes of Cepheid variables (as described in, e.g., Eddington 1926), nonradial modes have a pulsation axis. Originally, it was implicitly assumed that a star’s

pulsation axis coincides with its rotation axis, as it is about this axis that most stars deviate from spherical symmetry. It is still the case in modern asteroseismology (Aerts, Christensen-Dalsgaard & Kurtz 2010) that the starting point for modeling and inference is the assumption of the alignment of the pulsation and rotation axes.

However, stars can be distorted from spherical symmetry by other effects, primarily the presence of strong, global magnetic fields, and by tides arising from close companions. Therefore they may have pulsation axes not aligned with the rotational axis. The first stars found to pulsate about an axis other than the rotation axis were the rapidly oscillating Ap (roAp) stars (Kurtz 1982), which have primarily dipole magnetic fields that are inclined to the rotation axis. The combined effects of the rotation and magnetic fields lead to a pulsation axis that is inclined to the rotation axis and possibly offset from the stellar center. As the star rotates, the pulsation mode is then seen from varying ‘latitudinal view angles’¹, Θ , lead-

¹ Consider a star with a spin axis defined by \hat{s} and a pulsation axis, \hat{p} lying at an obliquity angle β with respect to the spin axis, and is viewed by a distant observer along a direction \hat{v} , such that $\hat{v} \cdot \hat{s} \equiv \cos i$, and i is the inclination angle. We define an angle Θ , the latitudinal view of the pulsation axis,

* E-mail: vzhang25@andover.edu

ing to modulation of both the observed pulsation amplitude and phase. This phenomenon is known as oblique pulsation.

Kurtz (1982) introduced the oblique pulsator model for the roAp stars, which has been refined over the last 40 years for asteroseismic inference. Holdsworth et al. (2021) provides the most up-to-date analysis of a large sample of roAp stars that were observed during the first two years of the Transiting Exoplanet Survey Satellite’s (*TESS*) mission (Ricker et al. 2015). A natural extension of the oblique pulsator model is to stars in close binary systems, wherein the pulsation axis could align with the tidal axis (the line joining the two stars). Since δ Sct stars are common upper main-sequence pulsators that are often found in close binary systems, it was no surprise that such “tidally tilted pulsators” (TTPs) were found in *TESS* data.

The first such system that exhibited TTPs, HD 74423, is a pair of nearly identical chemically peculiar λ Boo stars that nearly fill their Roche lobes in a 1.58-d binary (Handler et al. 2020). Only one of the stars is pulsating and in only one mode, which is unusual for a δ Sct star. The pulsation mode in HD 74423 is a highly distorted dipole mode that is, remarkably, largely confined to one hemisphere of the star. This discovery provided the impetus for the theoretical groundwork for understanding the interaction of pulsation and tidal distortion in close binary stars (Fuller et al. 2020). Such pulsations can provide significantly more information about the mode geometry than can be gleaned from ‘normal’ nonradial modes, and allows for the identification of the mode degree, ℓ , and azimuthal order, m (see, e.g., Reed, Brondel & Kawaler 2005).

The second TTP found was CO Cam, a marginal Am star in a 1.27-d binary with an undetected companion. It pulsates in at least four tidally tilted modes (Kurtz et al. 2020). Then the third discovery was TIC 63328020, which showed, for the first time, a tidally tilted sectoral ($|m| = \ell$) dipole mode (Rappaport et al. 2021). Previously, all identified modes in roAp stars had been zonal ($m = 0$) distorted dipole and quadrupole modes; this discovery allowed for further study of non-axisymmetric tidally tilted pulsations. The fourth discovery was HD 265435, a subdwarf B star which has been stripped of its H-rich envelope; this star has over 30 modes, of which at least 25 are tidally tilted (Jayaraman et al. 2022).

There has also been recent interest in less extreme examples of this phenomenon (the “tidally perturbed pulsators,” see, e.g., Southworth et al. 2020; Van Reeth et al. 2023; Johnston et al. 2023). Because our understanding of mode excitation, mode selection, and mode trapping in all pulsating stars remains rudimentary, discoveries of tidally tilted (and perturbed) pulsators with more, and different, kinds of pulsation modes provides further constraints on developing theory and asteroseismic inference.

However, the oblique pulsator model has been unable to explain certain observations of roAp stars. For instance, Kurtz et al. (2011) concluded that the two pulsation modes of the roAp star KIC 10192926 had different pulsation axes, both of which were inclined to the rotation axis. For another roAp star HD 6532, Kurtz & Holdsworth (2020) found that the single pulsation mode appeared to have a different pulsation axis when observed through the red *TESS* filter, compared to the pulsation axis derived from ground-based *B*-band observations. Because these two filters sample dif-

ferent atmospheric depths, perhaps the mode in this star has a complex three-dimensional geometry; this result may imply that different pulsation modes in a single star may be trapped in mode cavities with different pulsation axes. This effect remains unstudied.

In this work, we report the discovery of TIC 184743498, a close binary system whose primary star exhibits δ Sct pulsations over the frequency range 40–55 cycles d^{-1} . This star exhibits non-radial modes with pulsation axes aligned with the rotation axis, the tidal axis, and a third axis perpendicular to both of those. Thus, it is a tri-axial pulsator, the first of its kind. First, Section 2 describes how this source was discovered. Then, Section 3 discusses the data we used in addition to the photometry from *TESS*. In Section 4, we use the available observational data on this system to make robust estimates of the stellar parameters of the two binary stars, as well as a tertiary star, in TIC 184743498. The pulsation spectrum is discussed in Section 5, and the amplitudes and phases of these pulsations are reconstructed as a function of orbital phase in Section 6. The expected density of radial pulsation modes for TIC 184743498 is estimated in Section 7. We present in Section 8 a rudimentary perturbation model that can explain in a natural way how this star could have three different orthogonal pulsation axes. We summarize our results in Section 9, and look at future applications of our findings.

2 DISCOVERY

The first two TTPs discovered (Handler et al. 2020; Kurtz et al. 2020) were found serendipitously by visual examination of millions of *TESS* light curves from full frame images (Kristiansen et al. 2022). Since then, we have focused on *TESS* targeted stars with 120-s cadence calibrated light curves generated by the Science Processing Operations Center (SPOC; Jenkins et al. 2016). One of us (RJ) carried out a preliminary search for periodicities in all of the approximately 20,000 SPOC sources processed for each sector. A single summary sheet is generated for the approximately 1,000 stars from each sector that exhibit significant periodicity. The summary sheet includes plots of the raw light curve, the Fourier transform (FT) with various scalings, the inferred principal period, and a light curve folded about this period. The summary sheets also provide properties for each source taken from the *TESS* Input Catalog (TIC v8.0; Stassun et al. 2019), including the effective temperature, sky location, and estimated radius. Some of us then visually examine these summary sheets to search for interesting periodic stellar phenomena, including stellar pulsations in binary systems.

As a part of a continuing effort to identify TTPs, VZ visually inspected summary sheets for sources from the recent *TESS* Sectors 56–62, specifically looking for stars in binary systems whose FT displayed peaks at higher frequencies (typically $\gtrsim 15 \text{ d}^{-1}$). During visual inspection of the summary sheets from Sector 62, she found an interesting set of pulsations in TIC 184743498. In particular, she noticed high frequency pulsations between 40–55 d^{-1} in a ~ 1 d eclipsing close binary. Fig. 1 shows a small portion of the *TESS* light curve for TIC 184743498 covering about 3 d during Sector 62. Shallow eclipses, ellipsoidal light variations (ELV), and prominent pulsations are salient features of the raw light curve.

The top panel of Fig. 2 shows the Fourier amplitude spectrum of data from *TESS* Sectors 61 and 62 before any filtering. The FT clearly displays numerous orbital harmonics and a rich set of pulsations from TIC 184743498. The lower panels show the FT after the orbital harmonics have been removed, and then after the largest

as $-\hat{p} \cdot \hat{v}$. If \hat{p} revolves about \hat{s} by an angle ϕ due to either the rotation of the star or the orbital motion in the case of a tidally tilted pulsation axis, then it is straightforward to show that: $\cos \Theta = \cos i \cos \beta + \sin i \sin \beta \cos \phi$. If $\beta = 0$, i.e., no obliquity, then $\Theta = i$, a constant.

149 amplitude pulsations have been cleaned out. This ‘cleaning’ pro-
 150 cess for the Fourier transform is explained later in Section 5.

151 **3 DATA AVAILABILITY**

152 **3.1 TESS Data**

153 TIC 184743498 was observed by *TESS* at 30-min cadence in Sec-
 154 tor 8 (from 2019 May 16 to June 13), at 10-min cadence in Sectors
 155 34 and 35 (2021 January 14 to March 6), 200-s cadence in Sector
 156 61 (2023 January 18 to February 12), and 2-min cadence in Sector
 157 62 (2023 February 12 to March 10). This target was selected for
 158 2-min cadence observations because it was part of the *TESS* Candi-
 159 date Target List (CTL v8.01), a collection of bright ($T < 13$) stars
 160 in the *TESS* field of view that could host exoplanets. We accessed
 161 the data using the Python package `lightkurve` (Lightkurve Col-
 162 laboration et al. 2018). We used the Sector 61 and 62 data (200-s
 163 and 2-min cadence) for our principal pulsation analysis, but also
 164 utilised the Sector 34 and 35 data to confirm our findings based on
 165 the later sectors, and to better determine the orbital period. The Sec-
 166 tor 61 and 62 data, when combined, span 51 d and contains 28 700
 167 data points.

168 **3.2 Other Data**

169 We also made use of archival data from Gaia Data Release 3 (Gaia
 170 Collaboration et al. 2023), the Mikulski Archive for Space Tele-
 171 scopes (MAST)², the All-Sky Automated Survey for SuperNovae
 172 (ASAS-SN; Shappee et al. 2014; Kochanek et al. 2017), and the
 173 online VizieR SED viewer (Ochsenbein, Bauer & Marcout 2000)³.
 174 The basic archival parameters of TIC 184743498 from Gaia and
 175 MAST are summarized in Table 1. We used the ASAS-SN data
 176 primarily to obtain an accurate and independent value of the orbital
 177 period over a baseline of ~ 10 yr. The spectral energy distribution
 178 (SED) data were obtained from VizieR; these points were used in
 179 conjunction with other data to estimate the properties of the two
 180 stars in the binary in Sect 4.

181 Fortuitously, TIC 184743498 is one of the relatively rare
 182 double-line spectroscopic binaries in the Gaia data set (Katz et al.
 183 2023; Blomme et al. 2023). The Gaia K_1 and K_2 velocities, also
 184 listed in Table 1, are 119.3 and 154.9 km s⁻¹, respectively.

185 **3.3 Orbital period determination**

186 We determined the orbital period of TIC 184743498 using several
 187 different approaches.

188 First, using all five sectors of *TESS* data, we performed a Box
 189 Least Squares (BLS) analysis⁴ (Kovács, Zucker & Mazeh 2002).
 190 This method resulted in a period of 1.053 234 d. We also performed
 191 a BLS transform of the nearly 7,000 ASAS-SN archival flux points
 192 spanning 11 yr. The period derived from that data set is 1.053 238 d.
 193 The Gaia archives provide a period of 1.053 245 \pm 0.000 014 d,
 194 based on their RV solution to the orbit. These results are summa-
 195 rized in Table 2.

196 Additionally, we generated an eclipse timing variations (ETV)

Table 1. Properties of the TIC 184743498 System

Parameter	Value
RA (J2000) (h m s)	08:31:11.649
Dec (J2000) (° ' ")	-39:06:45.41
T^a	9.356 \pm 0.006
G^b	9.546 \pm 0.001
G_{BP}^b	9.6905 \pm 0.0035
G_{RP}^b	9.3181 \pm 0.0038
B^a	12.57 \pm 0.10
V^a	9.913 \pm 0.012
J^a	8.961 \pm 0.021
H^a	8.883 \pm 0.026
K^a	8.78 \pm 0.021
W1 ^c	8.767 \pm 0.023
W2 ^c	8.782 \pm 0.021
W3 ^c	8.753 \pm 0.025
W4 ^c	8.4 \pm 0.3
K_1 (km s ⁻¹) ^b	154.9 \pm 9.5
K_2 (km s ⁻¹) ^b	119.3 \pm 2.9
γ (km s ⁻¹) ^b	17.2 \pm 2.0
Distance (pc) ^b	393.3 \pm 4.8
μ_α (mas yr ⁻¹) ^b	-5.11 \pm 0.03
μ_δ (mas yr ⁻¹) ^b	+8.91 \pm 0.04

Notes. (a) MAST (<https://mast.stsci.edu/portal/Mashup/Clients/Mast/Portal.html>). (b) Gaia DR3: (Gaia Collaboration et al. 2023). (c) WISE point source catalog (Cutri & et al. 2013).

197 curve from the *TESS* data. The results are shown in Fig. 3. The
 198 reference period used to compute this ETV curve was 1.053 240
 199 d. The residuals from a linear ephemeris are nicely fitted with a
 200 quadratic term which can be described as a fractional rate of change
 201 in the orbital period of $\dot{P}_{orb}/P_{orb} \simeq -(1.030 \pm 0.013) \times 10^{-5}$
 202 yr⁻¹. This curvature in the ETV curve could represent either or-
 203 bital decay or a portion of a long-period orbit about a third body.
 204 Given that Gaia additionally reports an ‘acceleration’ solution for
 205 this object, this implies a non-linear component to the proper mo-
 206 tion (Halbwachs et al. 2023). This is consistent with orbital motion
 207 about a third body rather than orbital decay, and we adopt the for-
 208 mer hypothesis.

209 The mass of the third body necessary to induce this curvature
 210 in the ETV curve can be estimated to be in the range of ~ 0.7 -1.3
 211 M_\odot if the outer orbit has a period in the range ~ 2000 -6000 d. Such
 212 an orbital period would be consistent with (i) the fact that Gaia
 213 detects an accelerated astrometric motion, (ii) the duration of the
 214 Gaia observations, and (iii) the parabolic shape of the ETV curve,
 215 as opposed to a sinusoidal shape. With this possible mass range
 216 for the third star, we have to allow for the fact that it may make a
 217 non-negligible contribution to the system light.

218 **4 ESTIMATING THE STELLAR PARAMETERS**

219 We determined the stellar parameters of the stars in TIC 184743498
 220 with an SED fitting code that utilises the K velocities from Gaia
 221 (see Table 1) and parameter ratios from the light curve modeling
 222 code LIGHTCURVEFACTORY (see, e.g. Borkovits et al. 2019, 2020,
 223 and references therein).

224 The SED code is based on a Markov Chain Monte Carlo
 225 (MCMC; see, e.g., Ford 2005) fitting routine with only five ad-
 226 justable parameters: (i) the primary mass, M_1 , (ii) the secondary
 227 mass M_2 , (iii) the mass of the tertiary star in a wide outer orbit

² <https://mast.stsci.edu/portal/Mashup/Clients/Mast/Portal.html>

³ <http://vizier.cds.unistra.fr/vizier/sed/>

⁴ <https://exoplanetarchive.ipac.caltech.edu/cgi-bin/Pgram/nph-pgram>

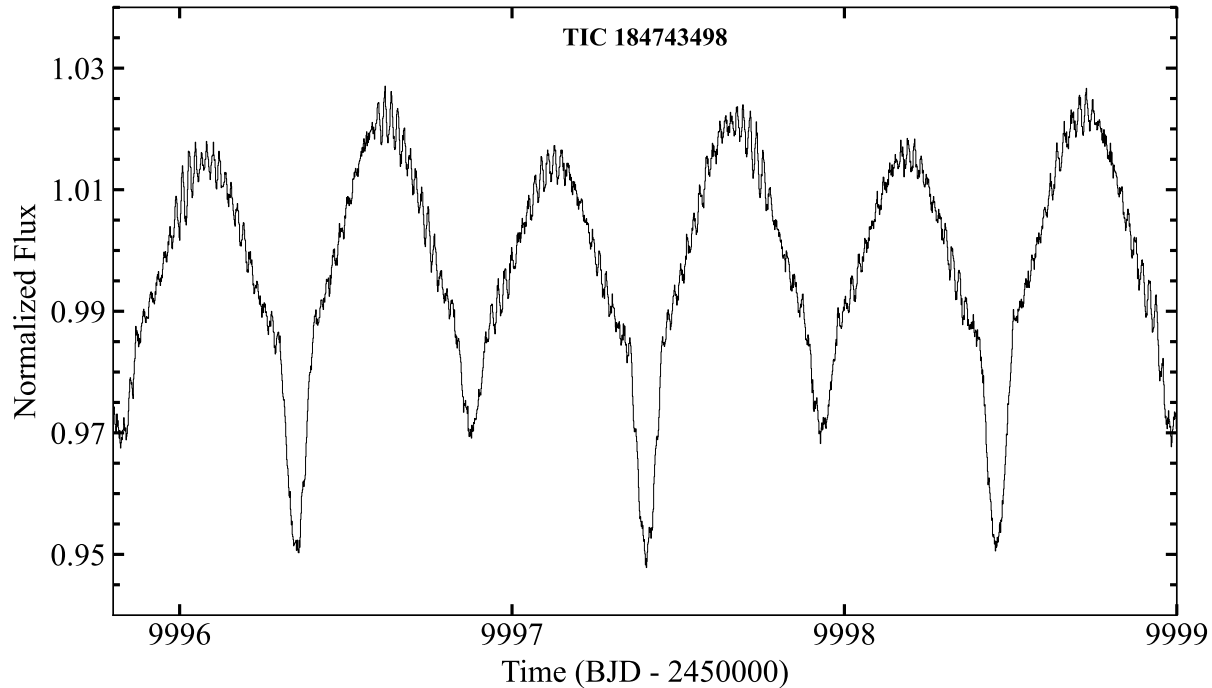


Figure 1. A portion of the Sector 62 TIC 184743498 light curve showing the eclipses, ellipsoidal light variations, and prominent pulsations. The *TESS* cadence for this sector was 120 s.

Table 2. Orbital Period of TIC 184743498

Source	Period
Gaia RV solution ^a	1.053 245 0 (140)
ASAS-SN ^b BLS	1.053 238 0 (30)
<i>TESS</i> BLS	1.053 272 0 (80)
<i>TESS</i> ^c ETV	1.053 240 0 (3)
<i>TESS</i> ^c ETV; $\dot{P}_{\text{orb}}/P_{\text{orb}}$ [yr^{-1}]	$-1.03 \pm 0.02 \times 10^{-5}$

Notes. (a) Gaia SB2C orbit (Katz et al. 2023; Blomme et al. 2023). Gaia also reports an acceleration solution (Halbwachs et al. 2023) which indicates non-linear proper motion. This is consistent with the non-linear ETV behavior we find with *TESS*. (b) ASAS-SN (Shappee et al. 2014; Kochanek et al. 2017). (c) See Fig. 3.

228 M_3 , (iv) the age of the system, τ , and (v) the interstellar extinction,
 229 A_V . The code models the following ‘input’ information: (i) 21 SED
 230 points, (ii) the K_1 and K_2 values with uncertainties from Gaia, (iii)
 231 two ratios ($T_{\text{eff},1}/T_{\text{eff},2}$ and $(R_1 + R_2)/a$) and the orbital inclina-
 232 tion angle, i , from a fit to the orbital light curve with LIGHTCURVE-
 233 FACTORY (Borkovits et al. 2019, 2020), and (iv) a set of stellar
 234 evolution tracks from MIST (Dotter 2016; Choi et al. 2016; Paxton
 235 et al. 2011; Paxton et al. 2015; Paxton et al. 2019), where a solar
 236 composition is assumed. We utilise the Castelli & Kurucz (2003)
 237 model stellar atmospheres for $4\,000 < T_{\text{eff}} < 10\,000$ K. The dis-
 238 tance is known with exquisite accuracy from Gaia parallax mea-
 239 surements.

240 The only constraints we have on the tertiary star are (i) from
 241 the total light of the system at each of the 21 SED points, and (ii) the
 242 fact that its mass is likely to be in the range of 0.7 to 1.3 M_{\odot} (based
 243 on the ETV curve, see Fig. 3 and the discussion of the figure). For
 244 the latter, we simply adopted a uniform prior on M_3 over the range
 245 0.5–1.6 M_{\odot} to be conservative.

246 Our approach follows that of Kurtz et al. (2020), Rappaport
 247 et al. (2021), and Rappaport et al. (2022). The MCMC code evalu-
 248 ates the following five parameters: M_1 , M_2 , M_3 , A_V , and the sys-
 249 tem age via the MIST equivalent evolutionary phase (EEP) of the
 250 primary star. The use of EEPs as a preferred sampling parameter—
 251 rather than directly sampling the stellar age—is described in detail
 252 in Kurtz et al. (2020). This procedure for the SED fitting has been
 253 utilised extensively in the study of numerous compact triples (Rap-
 254 paport et al. 2022, Rappaport et al. 2023). The validity of the results
 255 from those SED fits has been checked in a number of cases where
 256 there are several additional constraints on the system parameters.

257 At each step of the MCMC routine, the procedure is as fol-
 258 lows. The three masses and age of the binary (via the EEP) yield
 259 the stellar radii and T_{eff} values through the stellar evolution tracks.
 260 This, of course, assumes that the two EB stars have evolved in a
 261 coeval fashion and, in particular, that they have not previously ex-
 262 changed any mass. This, coupled with the model atmospheres and
 263 current value of A_V , allow for a model of the measured SED points.
 264 The χ^2 value from the SED fit is then registered. Additionally, the
 265 known orbital period and the two masses provide the semi-major
 266 axis of the system. When combined with the orbital inclination an-
 267 gle (provided by LIGHTCURVEFACTORY), this enables us to com-
 268 pute K_1 and K_2 , to compare with the measured Gaia values. The
 269 χ^2 values from the fit to the K velocities are also recorded. Finally,
 270 we check how well the model ratios of radii and T_{eff} match those
 271 provided by LIGHTCURVEFACTORY.

272 The light curve that we fit with LIGHTCURVEFACTORY is
 273 shown in Figure 4, and is based on Sectors 61 and 62 of the *TESS*
 274 data. Instead of the usual folded, or folded, binned, and averaged
 275 data, we use a light curve that is reconstructed from the first 45
 276 orbital harmonics⁵ that we fit for in the *TESS* data using a sim-

⁵ Here we used 45 harmonics as opposed to the 30 harmonics utilised for

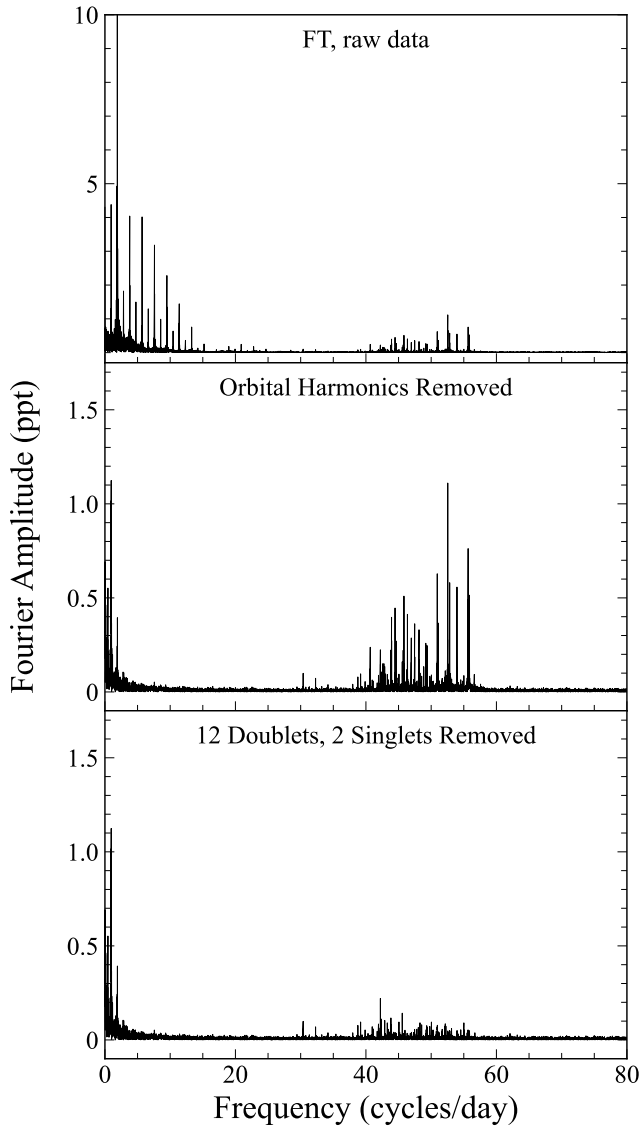


Figure 2. The Fourier amplitude spectrum of TIC 184743498. The panels highlight the amplitude spectrum after various stages of cleaning. The top panel shows the spectrum of the raw *TESS* light curve; the middle panel represents the spectrum following the removal of 30 orbital harmonics, while the bottom results from a further cleaning of the 13 pulsation modes discussed in the paper and listed in Table 4. Note the changes in amplitude scale between the upper and lower panels.

ilar technique to the one described later in Sect. 5. In principle, this synthetic light curve is the same as a folded, binned, and averaged light curve, except that (i) we avoid one of the pulsations that coincides with the 51st orbital harmonic and would otherwise appear in the folded light curve, and (ii) this also eliminates some of the high frequency noise that is not relevant to the shape of the light curve. The `LIGHTCURVEFACTORY` fit to the light curve of TIC 184743498 is shown in Figure 4 in red. The three key param-

cleaning the data prior to the FT (see Sect. 5). The 45 harmonics are used here to extract the maximum high-frequency content for the light curve without running into the 51st orbital harmonic which coincides with a pulsation frequency (see Table 4).

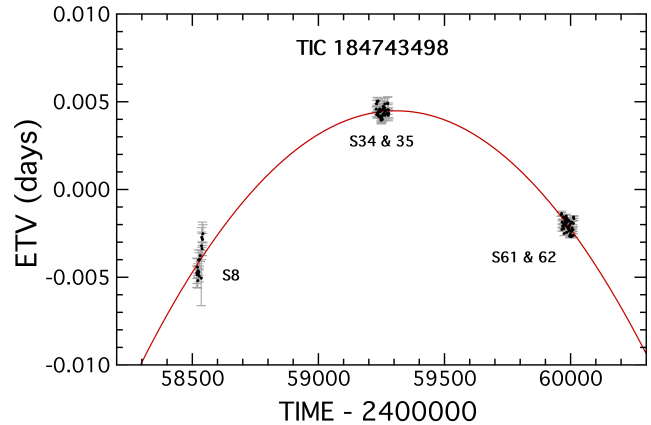


Figure 3. ETV curve based on 107 primary eclipse times from *TESS* Sectors 8, 34, 35, 61, and 62. The reference period for this analysis was 1.053 2400 d. The non-linear behavior is significant at the 80σ level.

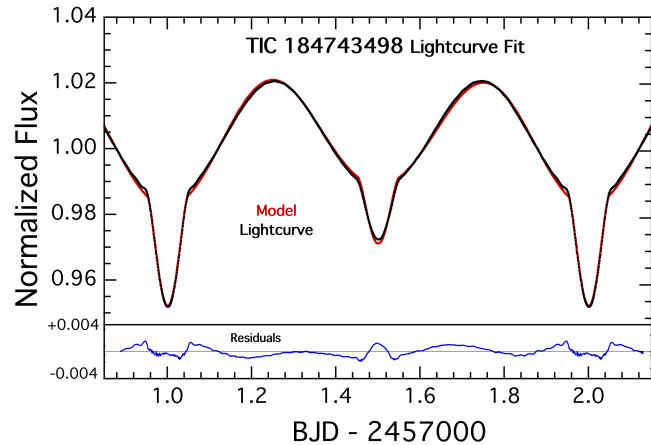


Figure 4. Model fit to the *TESS* sector 61 and 62 data. The black curve is the light curve reconstructed from the first 45 orbital harmonics. The red curve is a fitted model using `LIGHTCURVEFACTORY`. See text for details and references.

eters extracted from this fit are: $T_{\text{eff},1}/T_{\text{eff},2} = 1.241 \pm 0.010$, $(R_1 + R_2)/a = 0.500 \pm 0.025$, and $i = 65^\circ \pm 0.5^\circ$.

Figure 5 shows the results of the SED fitting. We plot the measured SED points in orange, the model SED of the primary star in red, that of the secondary in blue, and of the tertiary in green. The total flux is plotted in black. We find the following stellar parameters: $M_1 = 1.83 \pm 0.07 M_\odot$, $M_2 = 1.37 \pm 0.046 M_\odot$, $R_1 = 1.72 \pm 0.06 R_\odot$, and $R_2 = 1.35 \pm 0.06 R_\odot$. The parameters of the third star in the long outer-period orbit are less constrained, but are comparable to the properties of the secondary eclipsing binary (EB) star. The remaining fitted parameters can be found in Table 3.

We show in Fig. 6 the correlations in the MCMC posteriors for the mass vs. radius of the three stars in the TIC 184743498 system. The mass and radius of the primary are fairly well localized. By contrast, the secondary star in the EB shows a high degree of correlation between M_2 and R_2 . This results from the fact that the secondary is lower in mass and, at the age of the system, it is still firmly on the zero-age main sequence (ZAMS). The same is true for the tertiary star (in the wide outer orbit), but the degree of correlation between M_3 and R_3 appears even more extreme due to the

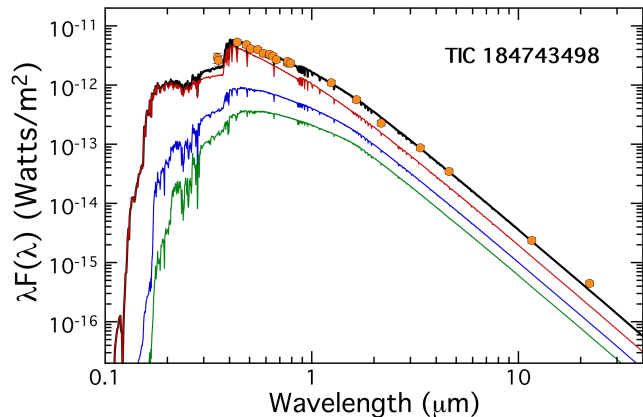


Figure 5. 21 SED points for TIC 184743498 (orange points) are fitted to stellar models for the three stellar components in this system. The contribution of the primary star is shown as a red curve, secondary is shown in blue, and tertiary is shown in green. The total model flux is given by the black curve. See text for the constraints that were used in the fit.

306 high degree of uncertainty in M_3 . The top panel of Fig. 6 shows the
307 1D posterior distributions for the stellar masses of each star.

308 5 PULSATIONS

309 We analyzed the pulsations of TIC 184743498 by applying a discrete
310 Fourier transform program to the raw *TESS* data. We performed FTs following various stages of cleaning: We first removed
311 the orbital harmonics from the data, and then removed the more prominent pulsation mode frequencies. As mentioned in Sect. 3.1,
312 we use Sectors 61 and 62 for pulsation analysis.
313

314 We started by subtracting the first 30 orbital harmonics from
315 the data, the highest frequency of which is near 28.5 d^{-1} . This was done via a simultaneous linear least-squares fit to 30 sines
316 and 30 cosines to represent the orbital modulations. We purposely stopped the cleaning at 30 orbital harmonics so as not to inadvertently
317 remove any natural pulsation frequencies that happen to lie near an orbital harmonic or are, in fact, tidally excited at exactly
318 that harmonic. The amplitudes of the orbital harmonics above this frequency are small enough so that they are not likely to be confused
319 with stellar pulsations. Furthermore, possible residual orbital harmonics will have a phase in an echelle diagram (see below) close
320 to 0 or 1, and will therefore be easily recognized. The middle panel of Fig. 2 shows the resultant FT in the frequency range from 0 to
321 80 d^{-1} after 30 orbital harmonics have been removed. We see a rich spectrum of pulsations within the range of $38\text{--}56 \text{ d}^{-1}$. The bottom
322 panel of Fig. 2 shows the transform after removing the 13 most prominent frequencies (enumerated in Table 4).
323

324 To better visualize the organization of the pulsations in
325 TIC 184743498, we generated an echelle diagram. Such a diagram plots the frequency of a pulsation on the y-axis against the echelle
326 phase on the x-axis; this so-called “echelle phase” is the pulsation frequency modulo the orbital frequency, normalized by the orbital
327 frequency. In the creation of an echelle diagram, we set a threshold for the minimum Fourier amplitude ($\gtrsim 7\sigma$), such that only highly
328 significant peaks are represented.
329

330 Fig. 7 displays the echelle diagram for TIC 184743498 following the removal of 30 orbital harmonics. The amplitude threshold
331 is 0.05 ppt ($\sim 7\sigma$). We limit the echelle diagram to the relevant frequency range where the vast majority of peaks are located, and
332

Table 3. Derived Parameters for the TIC 184743498 System

Input Constraints	SED + RVs ^a
Period (days)	1.053236
K_1 (km s^{-1}) ^b	119.3 ± 2.9
K_2 (km s^{-1}) ^b	154.9 ± 9.5
Spectral	21 SED points ^c
Stellar evolution tracks	MIST ^d
Distance (pc) ^b	374 ± 6
$(R_1 + R_2)/a$ ^e	0.500 ± 0.025
$T_{\text{eff},1}/T_{\text{eff},2}$ ^e	1.241 ± 0.030
Stellar inclination angle ^e	$65.2^\circ \pm 0.5^\circ$
Derived Parameters	SED + RVs ^a
M_1 (M_\odot)	1.83 ± 0.07
M_2 (M_\odot)	1.37 ± 0.06
M_3 (M_\odot)	1.23 ± 0.09
R_1 (R_\odot)	1.72 ± 0.06
R_2 (R_\odot)	1.35 ± 0.06
R_3 (R_\odot)	1.19 ± 0.11
$T_{\text{eff},1}$ (K)	8500 ± 300
$T_{\text{eff},2}$ (K)	6870 ± 200
$T_{\text{eff},3}$ (K)	6450 ± 270
$L_{1,\text{bol}}$ (L_\odot)	14.1 ± 2.2
$L_{2,\text{bol}}$ (L_\odot)	3.7 ± 0.8
$L_{3,\text{bol}}$ (L_\odot)	2.3 ± 0.8
a (R_\odot)	6.41 ± 0.09
R_1/R_L	0.66 ± 0.02
age (Myr)	460 ± 120
A_V	0.35 ± 0.10

Notes. (a) MCMC fits to the measured RV amplitude plus the SED points. The assumption is made that the two stars are coeval in their evolution, and have not exchanged any mass. (b) Gaia (Katz et al. 2023) (c) VizieR: (Ochsenbein, Bauer & Marcout 2000); A.-C. Simon & T. Boch: <http://vizier.unistra.fr/vizier/sed/>. (d) MIST (Dotter 2016; Choi et al. 2016). (e) LIGHTCURVEFACTORY (Borkovits et al. 2019, 2020) fit to the *TESS* orbital light curve.

size each dot by linearly scaling the Fourier amplitude to emphasize the more prominent peaks. We see 11 doublets (also referred to as “multiplets”), which are a vertically aligned pair of filled circles separated by twice the orbital frequency. These doublets are encircled in red ellipses and labeled by increasing frequency. These results are also tabulated in Table 4. We encircle two singlets in blue ellipses.

For each multiplet, we find the frequencies of the observed peaks (marked by ellipses in the echelle diagram) and then calculate the inferred (unseen) central frequency at which the star is actually pulsating. All the measured and inferred frequencies of the multiplets and singlets are summarized in Table 4.

6 RECONSTRUCTING THE PULSATION AMPLITUDES AND PHASES

The amplitudes and phases of the elements of each of the 11 pulsation doublets (see Fig. 7) carry all the information about a particular pulsation mode that can be extracted from the *TESS* data. However, the specific pulsation modes cannot be entirely inferred merely by inspecting the echelle diagram. In this regard, it is extremely useful to reconstruct the behavior of the pulsation amplitudes and phases as a function of orbital phase. To do this, we analytically recon-

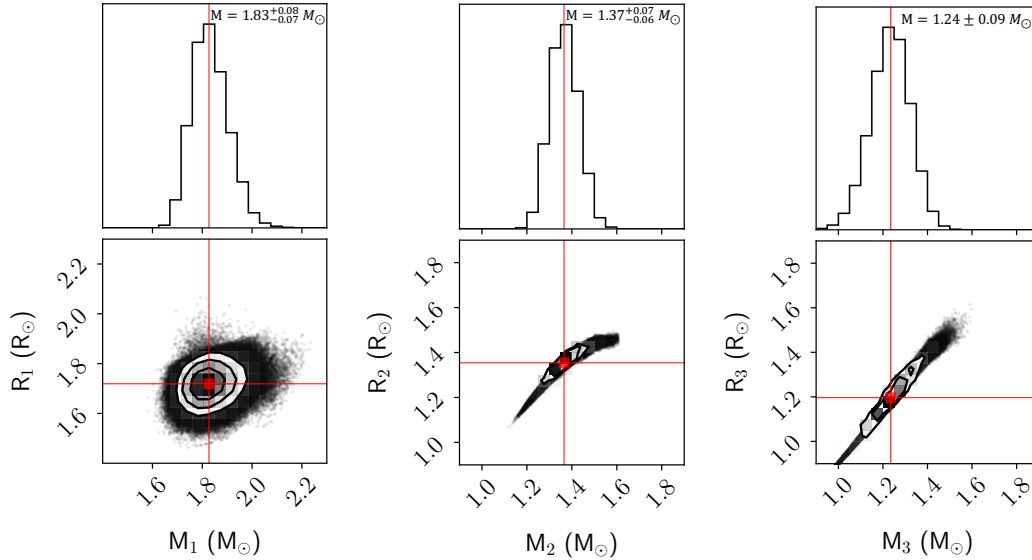


Figure 6. Correlations between the mass and radius of the three stars in the TIC 184743498 system, as well as posterior distributions of the masses. The mass and radius of the secondary EB star and the tertiary are well correlated because these stars are still on the zero-age main sequence, where there is a one-to-one correspondence between mass and the other stellar parameters.

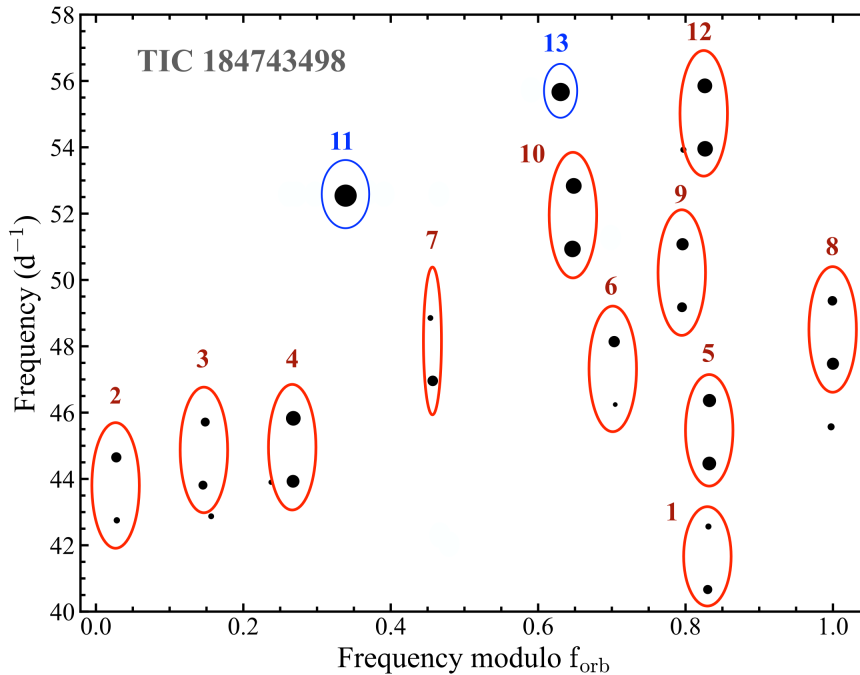


Figure 7. Echelle diagram following a cleaning of the data that removed the first 30 orbital harmonics. This diagram shows pulsation peaks as a function of their frequency and echelle phase, i.e., the normalized pulsation frequency modulo the orbital frequency. Points are sized linearly by their Fourier amplitude. Red ellipses mark the pulsation multiplets that we have identified. These are numbered according to increasing central frequency to match the notation in Table 4.

365 struct the amplitudes and phases of 9 of the doublets in the echelle 373
 366 diagram (all except for doublets 6 and 7, whose phase and ampli- 374
 367 tude behavior are not robustly characterized). We follow the for- 375
 368 malism for reconstructing multiplets provided in Eqns. (2)-(6) of 376
 369 Jayaraman et al. (2022). 377

370 To be conservative, we force fit a quintuplet of components to 378
 371 each doublet, at frequencies ν_0 , $\nu_0 \pm \nu_{\text{orb}}$ and $\nu_0 \pm 2\nu_{\text{orb}}$. If at one or 379
 372 more of the 5 frequencies there is no significant FT amplitude, then 380

the only contribution to the reconstruction will be a small amount of 373
 added noise. However, there may be a weak (albeit real) signal 374
 there which did not surpass the echelle threshold, and we cannot 375
 neglect its contribution. Note that we use the same reconstruction 376
 process for all the pulsation modes, regardless of spacing or status 377
 as a singlet or doublet. Finally, we chose the same reference eclipse 378
 time, t_0 , as was used in the pulsation analysis in Section 5. 379

Fig. 8 shows the amplitude-phase plots for the central fre-

Table 4. Dominant Pulsation Frequencies in the TIC 184743498 System

Mode Name	Frequency ^a d ⁻¹	Amplitude ppt	Phase ^b radians	Echelle Phase cycles
Uncertainty:	0.0006	0.007	~0.03	~0.002
$\nu_1 - \nu_{\text{orb}}$	40.6653	0.234	-1.10	0.830
ν_1	(41.6152)			
$\nu_1 + \nu_{\text{orb}}$	42.5651	0.143	-1.23	0.831
$\nu_2 - \nu_{\text{orb}}$	42.7525	0.149	-0.60	0.028
ν_2	(43.7016)			
$\nu_2 + \nu_{\text{orb}}$	44.6507	0.274	-0.54	0.028
$\nu_3 - \nu_{\text{orb}}$	43.8129	0.225	+1.45	0.145
ν_3	(44.7638) ^c			
$\nu_3 + \nu_{\text{orb}}$	45.7147	0.225	+1.71	0.148
$\nu_4 - \nu_{\text{orb}}$	43.9289	0.399	-2.20	0.267
ν_4	(44.8785)			
$\nu_4 + \nu_{\text{orb}}$	45.8282	0.507	-2.19	0.268
$\nu_5 - \nu_{\text{orb}}$	44.4652	0.449	-2.51	0.832
ν_5	(45.4147)			
$\nu_5 + \nu_{\text{orb}}$	46.3643	0.419	+0.61	0.832
$\nu_6 - \nu_{\text{orb}}$	46.2429	0.118	-0.55	0.705
ν_6	(47.1917)			
$\nu_6 + \nu_{\text{orb}}$	48.1405	0.323	+2.58	0.703
$\nu_7 - \nu_{\text{orb}}$	46.9572	0.288	-2.05	0.457
ν_7	(47.9047)			
$\nu_7 + \nu_{\text{orb}}$	48.8532	0.137	-1.64	0.454
$\nu_8 - \nu_{\text{orb}}$	47.4729	0.362	-2.00	1.000
ν_8	(48.4219) ^d			
$\nu_8 + \nu_{\text{orb}}$	49.3710	0.247	+1.36	0.999
$\nu_9 - \nu_{\text{orb}}$	49.1773	0.259	-2.05	0.795
ν_9	(50.1271)			
$\nu_9 + \nu_{\text{orb}}$	51.0769	0.368	-2.06	0.796
$\nu_{10} - \nu_{\text{orb}}$	50.9351	0.630	+0.63	0.647
ν_{10}	(51.8853)			
$\nu_{10} + \nu_{\text{orb}}$	52.8356	0.579	-2.53	0.648
ν_{11}	52.5418	1.113	...	0.339
$\nu_{12} - \nu_{\text{orb}}$	53.9543	0.563	+1.42	0.826
ν_{12}	(54.9036)			
$\nu_{12} + \nu_{\text{orb}}$	55.8529	0.513	-1.73	0.827
ν_{13}	55.6671	0.765	...	0.631

Notes. (a) A least-squares fit of the 13 most prominent pulsation modes. Numbers in parentheses are the unseen central frequencies of the doublets, and hence are the actual mode frequencies. (b) The zero point for the phases has been chosen to be the time of the primary eclipse: $t_0 = \text{BJD } 2459988.9789$. For later reference in the paper, we note that phase differences between the two components with values near zero correspond to what we call a $Y_{10,x}$ mode, while those with phase differences closer to π are called $Y_{10,y}$ modes (see Eqns. (9) and (10)). (c) This central frequency was likely directly observed at $\nu = 44.7594 \text{ d}^{-1}$, amplitude = 0.073 ppt, and echelle phase 0.142. (d) This has an echelle phase that is completely consistent with an orbital harmonic, but its amplitude is too high for that to be the case. Thus, this is either a natural frequency that just happens to coincide with an orbital harmonic to within the uncertainties (0.4% random chance), or is a mode driven by the orbit. Moreover, the echelle diagram (Fig. 7) appears to show a third component at $\nu = 45.5715 \text{ d}^{-1}$, but we have shown from the use of all the data, including Sectors 34 and 35, that this is not part of the same doublet.

381 frequencies ν_1 though ν_4 , and ν_9 , in Table 4, and Fig. 9 gives the
 382 amplitude-phase plots for frequencies ν_5 , ν_8 , ν_{10} , and ν_{12} . The am-
 383 plitude reconstructions are shown in the left panels, while the phase
 384 variation over the orbit is displayed in the right panels. During the
 385 reconstruction, we scaled the pulsation amplitude up by a factor of

2 for better visibility. The two different figures represent different
 kinds of pulsation modes.

We have collected in Fig. 8 all five doublet pulsation modes
 whose amplitude maxima occur at the eclipses and have π phase
 jumps near the ellipsoidal light variation (ELV) peaks. By contrast,
 Fig. 9 displays all four doublets whose amplitude maxima occur

at the ELV peaks and have π phase jumps near the eclipses. The pulsation modes in Fig. 8 can all be described by dipole modes of the form Y_{10} , namely with $\ell = 1$ and $m = 0$, if the pulsation axis has been tidally tilted into the orbital plane and follows the tidal axis as it orbits with the binary. At low inclination angles, even lower than the 65° for this system, the doublet nature of such a pulsation mode along the tidal axis will be preserved (see, e.g., Reed, Brondel & Kawaler 2005). This means no central peak will appear in the echelle diagram, and indeed this is the case as we look at doublets for $\nu_1, \nu_2, \nu_3, \nu_4$, and ν_9 in Fig. 7. We hereafter refer to these as $Y_{10,x}$ modes.

By contrast, the reconstructions in Fig. 9 all have pulsation maxima and π phase shifts at orbital phases that are 90° displaced from those in Fig. 8. Thus, one might be tempted to explain these pulsations as dipole modes of the form Y_{11} ($\ell = 1$, and $|m| = 1$), again for a tidally tilted pulsation axis. However, for this system's relatively low orbital inclination angle, strong central frequency components must appear in the echelle diagram for Y_{11} modes, yet we do not see such a central component for any of the doublets in Fig. 7. This is equivalent to noting that a Y_{11} mode tilted along the tidal axis which, in turn, is at an inclination of 65° , could not have zero pulsation amplitude at the eclipses – as we see in Fig. 9.

In Fig. 10, we show explicitly how the FT of a tidally tilted Y_{11} mode varies with orbital inclination angle. As is clear from the figure, a significant central peak begins to appear at $i \lesssim 80^\circ$, and is nearly equal to the split sidelobes by $i = 60^\circ$. Thus, it would be implausible to have such a mode produce the types of doublets we see in Fig. 7, which have neither a strong central peak nor non-trivial pulsations at the eclipses.

We therefore propose that the four modes shown in Fig. 9 are actually $Y_{10,y}$ modes with the pulsation axis along the “ y -axis”, which is perpendicular to the tidal axis (x) and the orbital angular momentum axis (z). This hypothesis resolves the issue of the missing central component of the doublets, and zero pulsation amplitude at the eclipses, while being fully consistent with the pulsation amplitudes and phase shifts with respect to orbital phase. Thus, this represents the first discovery of a stellar pulsator with a pulsation axis along the y direction.

In the same spirit as the above hypothesis, we also propose that the two singlets found in this source and listed in Table 4 are Y_{10} modes with a pulsation axis along z . Given that their two frequencies are 52.5411 and 55.6664 d^{-1} , with a difference of $\sim 3 \text{ d}^{-1}$, the interval here is too narrow to host radial modes with such frequencies. This hypothesis is further explained in Section 7.

Finally, we note that the modes with frequencies ν_6 and ν_7 , which do not appear in Figs. 8 and 9, each have markedly different amplitudes for their two doublet peaks. However, the reconstructed pulsation amplitude and phase behavior with orbital phase of ν_6 very closely resembles those in Fig. 9, i.e., $Y_{10,y}$ modes, while ν_7 would be associated with those modes in Fig. 8, i.e., $Y_{10,x}$. Thus, these two doublets are likely distorted Y_{10} tidally tilted modes.

7 DENSITY OF RADIAL MODELS

In Sect. 5, we reported two singlets spaced in frequency by only $\sim 3 \text{ d}^{-1}$. In the presence of tidally tilted pulsations, such singlets are most readily explained by radial modes, as their pulsational amplitudes and phases will not be modulated over the orbit. We investigate whether radial modes are a plausible interpretation for those two frequencies.

To this end, we computed single-star pulsational models using

the latest version of the Warsaw-New Jersey stellar evolution and pulsation code (e.g., Pamyatnykh et al. 1998), for a solar chemical composition (Asplund et al. 2004) and a rotational velocity of 100 km s^{-1} at the ZAMS. We evaluated the frequency differences of consecutive radial overtones of modes in the domain of $50 - 60 \text{ d}^{-1}$ along each evolutionary track and determined the locations of models that would reproduce the observed frequency difference $\nu_{13} - \nu_{11}$ at the radial mode frequency closest to ν_{13} . Figure 11 shows the loci of those models, as well as of the stellar components of the TIC 184743498 system, in a theoretical Hertzsprung-Russell Diagram (HRD).

Inspection of Fig. 11 clearly demonstrates that (i) only the primary star (star 1) is expected to exhibit δ Scuti type pulsations, and (ii) frequencies ν_{11} and ν_{13} cannot both be radial modes, as all stellar models that produce consecutive radial modes that are closely spaced in frequency are too evolved. Models producing ν_{11} and ν_{13} as non-consecutive radial modes would be even more evolved.

Additionally, we look at the expected pulsation spectrum of dipole modes of a single star with the parameters we derived for the primary star in the TIC 184743498 system. The corresponding pulsation frequencies were computed analogously to those of the radial modes with the Warsaw-New Jersey code, for a model with $\log T_{\text{eff}} = 3.9206$, and $\log L = 1.1302$ (cf. Table 3). Nonradial mode rotational frequency splittings were computed to first order in stellar rotation frequency. The schematic frequency spectrum so derived is shown in Fig. 12.

Evidently, the expected spectrum of axisymmetric dipole modes (Y_{10}) is not dense enough to explain all the observed frequencies. As the underlying model is fairly unevolved, no avoided crossings (mixed modes) are present in the theoretical frequency spectrum; the modes shown here are of radial overtone 5 to 7. However, by including sectoral dipole modes ($Y_{1\pm 1}$), the density of the observed apparent dipole frequency spectrum can be explained.

The above arguments lead us to the conclusion that at least one of the ν_{11} and ν_{13} singlets, and possibly both, must indeed be a Y_{10} mode with a pulsation axis along z , i.e., $Y_{10,z}$ modes.

8 TIDAL MODE-COUPLING MODELS

As suggested in Section 5, the pulsations of TIC 184743498 can be best explained by three different pulsation axes. In particular, it appears that there are five dipole Y_{10} modes with pulsation axis aligned with the tidal (or x axis), while four are dipole Y_{10} modes with a pulsation axis aligned along the y axis (i.e., in the orbital plane, but orthogonal to the x axis). Here we justify this hypothesis with a straightforward physical argument.

Rather than assuming that tidal distortion aligns pulsations with the tidal axis, we show that tidal coupling between modes naturally produces modes with three different pulsation axes. Consider an $\ell = 1$ triplet, now using the rotation/orbital axis as a reference axis. We formally define the x -axis in the direction of the companion, the z -axis in the direction of the spin/orbital angular momentum, with the y -axis lying in the orbital plane. The tidal distortion is dominated by the $\ell = m = 2$ component of the tidal potential, which couples the $\ell = m = 1$ mode with the $\ell = 1, m = -1$ mode. Writing out the coupled eigensystem for this mode triplet

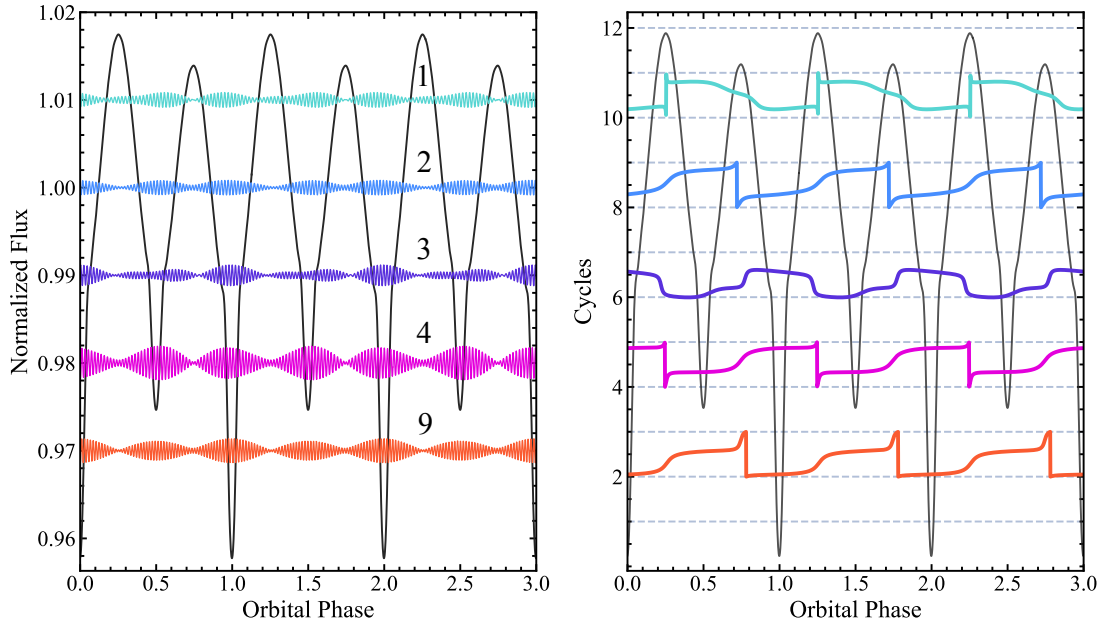


Figure 8. Left and right panels: The reconstructed pulsation amplitude and phase variations as a function of orbital phase for the five doublets that we have classified as $Y_{10,x}$ pulsation modes with a pulsation axis along the tidal axis (ν_1 through ν_4 and ν_9); the frequencies are listed in Table 4. The reconstructed pulsations have been vertically offset from each other by 0.01 for clarity, and each pulsation amplitude has been doubled from its actual value to make it more visible. The phase reconstructions are offset vertically from one another by 2 cycles. We label each reconstructed mode with its frequency numbering. The black curve superposed on the plots is the reconstructed orbital modulation. See text for details of the reconstructions.

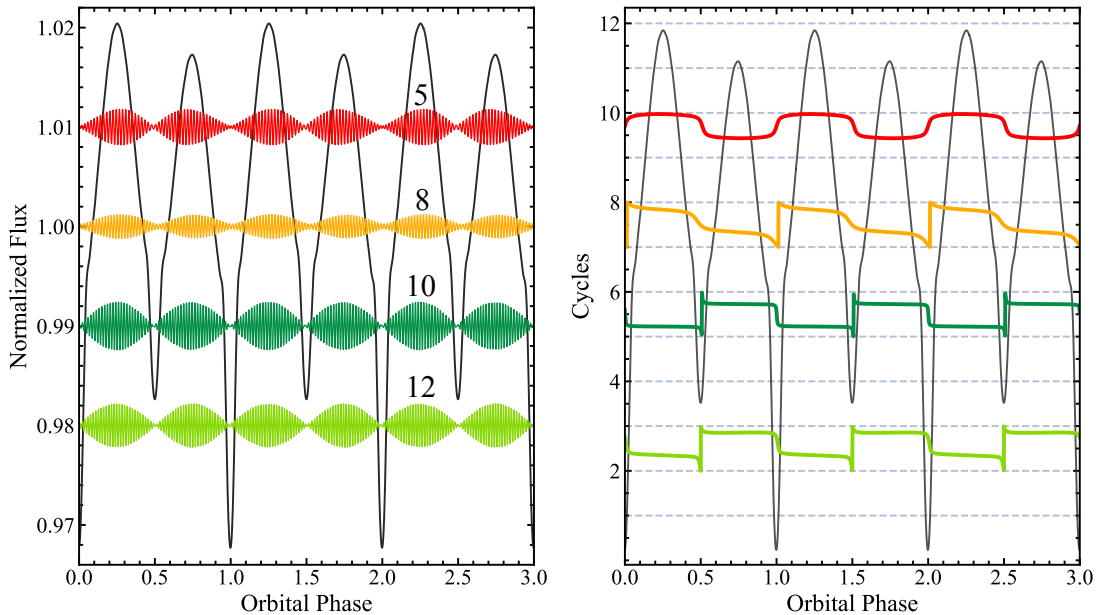


Figure 9. Left and right panels: The reconstructed pulsation amplitude and phase variations as a function of orbital phase for the four doublets that we have classified as $Y_{10,y}$ pulsation modes with a pulsation axis along the y direction (perpendicular to the tidal and angular momentum axes). The frequencies ν_5 , ν_8 , ν_{10} , and ν_{12} are listed in Table 4. The reconstructed pulsations have been vertically offset from each other by 0.01 for clarity, and each pulsation amplitude has been doubled from its actual value to make it more visible. The phase reconstructions are offset vertically from one another by 2 cycles. We label each reconstructed mode with its frequency numbering. The black curve superposed on the plots is the reconstructed orbital modulation. See text for details of the reconstructions.

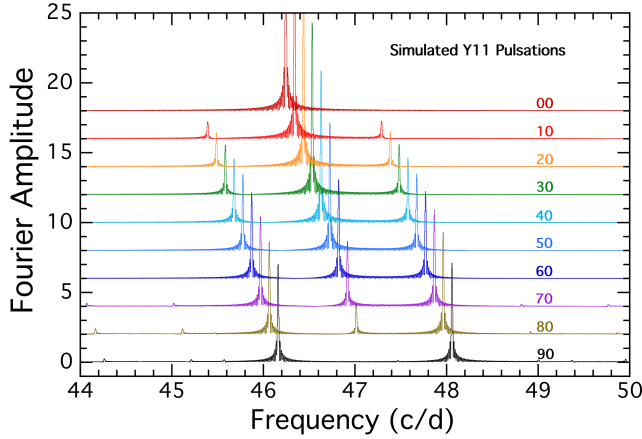


Figure 10. Fourier transforms of simulated pulsation for a mode Y_{11} with a pulsation axis along the tidal axis of the binary (x -axis). The orbital inclination angle for each simulation is labeled in color. The curves for different inclinations are separated both vertically and horizontally for clarity. A central peak starts to appear at $i \lesssim 80^\circ$, and is nearly equal to the split sidelobes by $i = 60^\circ$.

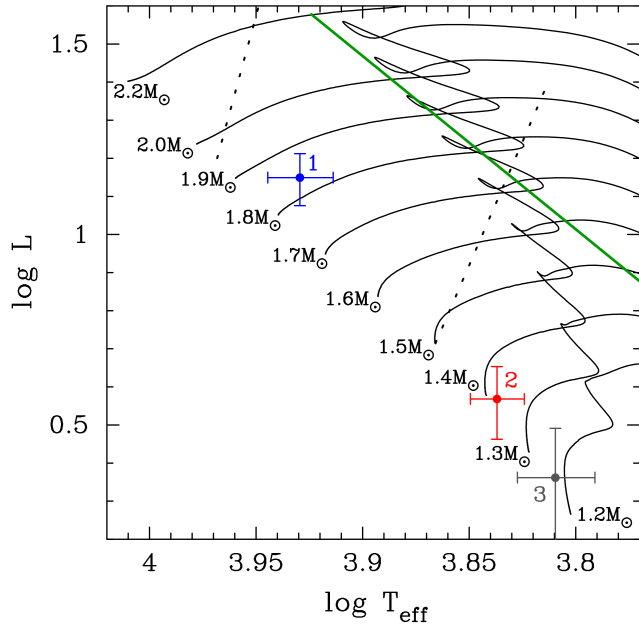


Figure 11. Theoretical HRD with the locations of the three components of TIC 184743498 (stars 1, 2, and 3) indicated. The evolutionary tracks are the same as were used in the SED fit shown in Fig. 5. The dashed black lines are the observed boundaries of the δ Scuti star instability strip (Murphy et al. 2019). The green line connects models that best represent the observed pulsation frequencies ν_{11} and ν_{13} with radial modes.

(i.e., Eqn. 8 of Fuller et al. 2020), we find

$$\begin{aligned} & \begin{bmatrix} \omega_\alpha^2 + \delta\omega_0^2 & 0 & 0 \\ 0 & \omega_\alpha^2 + \delta\omega_1^2 & \delta V_{1-1} \\ 0 & \delta V_{1-1} & \omega_\alpha^2 + \delta\omega_{-1}^2 \end{bmatrix} \begin{bmatrix} a_0 \\ a_1 \\ a_{-1} \end{bmatrix} \\ &= \omega^2 \begin{bmatrix} 1 & 0 & 0 \\ 0 & 1 & \delta T_{1-1} \\ 0 & \delta T_{1-1} & 1 \end{bmatrix} \begin{bmatrix} a_0 \\ a_1 \\ a_{-1} \end{bmatrix} \end{aligned} \quad (1)$$

Here, ω is the frequency of a mode of the coupled system, ω_α^2 is the unperturbed frequency of the mode triplet, and δV_{1-1} and δT_{1-1}

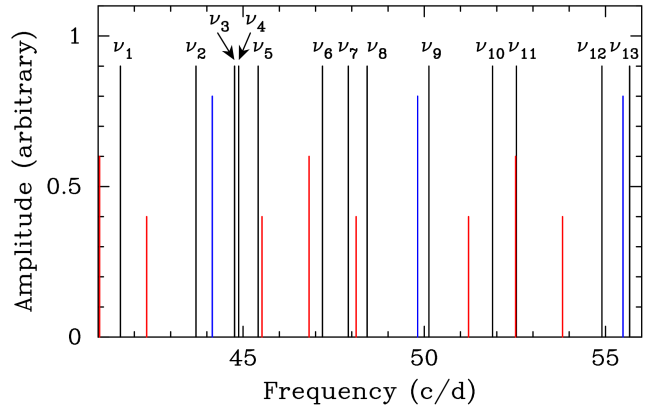


Figure 12. Schematic pulsation frequency spectrum of TIC 184743498. The black lines denote the observed centroid mode frequencies, whereas the blue lines indicate the theoretical model radial-mode frequencies. Red lines represent theoretical dipole mode frequencies, with those of ‘amplitude’ 0.6 corresponding to $m = 0$ and those of ‘amplitude’ 0.4 to $|m| = 1$.

are tidal coupling coefficients. The values of \mathbf{a} are the relative contributions of the Y_{1m} components of the $\ell = 1$ triplet to the new eigenfunctions of the coupled triplet. Solving the eigensystem of Eqn. 1 yields the three mode frequencies ω^2 and eigenfunctions \mathbf{a} of the perturbed mode triplet.

Since the $m = 0$ mode remains uncoupled in this simple scenario, its eigenfrequency is slightly perturbed and its eigenfunction remains unchanged. It is an $m = 0$ mode about the z -axis, i.e., the spin/orbital axis. The $m = \pm 1$ modes are coupled, however, and the eigensystem of Eqn. 1 for those modes reduces to

$$\begin{bmatrix} 1 & -\delta T_{1-1} \\ -\delta T_{1-1} & 1 \end{bmatrix} \begin{bmatrix} \omega_\alpha^2 + \delta\omega_1^2 & \delta V_{1-1} \\ \delta V_{1-1} & \omega_\alpha^2 + \delta\omega_{-1}^2 \end{bmatrix} \begin{bmatrix} a_1 \\ a_{-1} \end{bmatrix} \quad (2)$$

$$\simeq \begin{bmatrix} \omega_\alpha^2 + \delta\omega_1^2 & \delta\omega_{\text{tide}}^2 \\ \delta\omega_{\text{tide}}^2 & \omega_\alpha^2 + \delta\omega_{-1}^2 \end{bmatrix} \begin{bmatrix} a_1 \\ a_{-1} \end{bmatrix} \quad (3)$$

$$\simeq \omega^2 \begin{bmatrix} a_1 \\ a_{-1} \end{bmatrix}, \quad (4)$$

where

$$\delta\omega_{\text{tide}}^2 = \delta V_{1-1} - \omega_\alpha^2 \delta T_{1-1}. \quad (5)$$

Here, we have assumed small perturbations such that $\delta\omega_1^2$, $\delta\omega_{-1}^2$, $\delta V_{1-1} \ll \omega_\alpha^2$, and $\delta T_{1-1} \ll 1$, and we have dropped second-order terms in these small quantities.

In the limit that $\delta\omega_{\text{tide}}^2 \ll \delta\omega_1^2 - \delta\omega_{-1}^2$, then this eigensystem reduces to the uncoupled system, with frequencies $\omega^2 = \omega_\alpha^2 + \delta\omega_1^2$ and $\omega^2 = \omega_\alpha^2 + \delta\omega_{-1}^2$, and eigenfunctions of Y_{11} and Y_{1-1} . All modes have the z -axis as their pulsation axis.

However, in the limit of strong tidal coupling such that $\delta\omega_{\text{tide}}^2 \gg \delta\omega_1^2 - \delta\omega_{-1}^2$, solving the eigensystem yields the new mode eigenfrequencies

$$\omega_\pm^2 = \omega_\alpha^2 \pm \delta\omega_{\text{tide}}^2. \quad (6)$$

with corresponding eigenvectors

$$\mathbf{a}_\pm = \begin{bmatrix} 0 \\ 1 \\ \pm 1 \end{bmatrix} \quad (7)$$

Hence, the new mode eigenfunctions are equal superpositions of $Y_{1,1}$ and $Y_{1,-1}$, with angular flux perturbation patterns

$$\delta F_\pm \propto [Y_{11}(\theta, \phi) \pm Y_{1-1}(\theta, \phi)] e^{-i\omega_\pm t}. \quad (8)$$

Some algebra shows that the spatial/time dependence of these two modes are

$$\begin{aligned} \delta F_+ &\propto \sin \theta \cos \phi \cos(\omega_+ t) \\ &\propto x \cos(\omega_+ t) \\ &\propto Y_{10,x} \cos(\omega_+ t) \end{aligned} \quad (9)$$

and

$$\begin{aligned} \delta F_- &\propto \sin \theta \sin \phi \sin(\omega_- t) \\ &\propto y \cos(\omega_- t) \\ &\propto Y_{10,y} \cos(\omega_- t) \end{aligned} \quad (10)$$

Note also that the $m = 0$ mode has

$$\begin{aligned} \delta F_0 &\propto \cos \theta \cos(\omega_\alpha t) \\ &\propto z \cos(\omega_\alpha t) \\ &\propto Y_{10,z} \cos(\omega_\alpha t) \end{aligned} \quad (11)$$

The extra subscripts on the Y_{10} spherical harmonics (x, y, z) refer to the axis with respect to which the spherical harmonic is defined. Note that neither of the modes in Eqn. 9 or Eqn. 10 propagates around the equator like uncoupled $m = \pm 1$ modes. Instead, both modes are standing modes, aligned with the x - and y -axes. The $m = 0$ mode is a standing mode aligned with the z -axis. Thus, we find that strong tidal coupling naturally transforms an $\ell = 1$ dipole triplet of states to a set of Y_{10} modes around three orthogonal axes. Hence, tidally coupled $\ell = 1$ modes can behave identically to the tri-axial pulsation behavior necessary to explain the observations of TIC 184743498.

Tidal coupling will have a similar effect on $\ell = 2$ modes, coupling the Y_{21} and Y_{2-1} modes into a perturbed doublet, and the Y_{22} , Y_{20} , and Y_{2-2} modes into a triplet. This will produce more complicated spatial patterns than those discussed above, with different amplitude/phase modulation over the orbit. We plan to examine these signatures in future work and simultaneously search for these signatures in other stars in the *TESS* data.

As mentioned above, tidal coupling also couples modes of different ℓ , which is not accounted for above. For weak tidal distortion, the $\ell = 2$ component of the tidal distortion dominates, such that coupling between modes differing by $\Delta\ell = 2$ and $\Delta\ell = 0$ is strongest. For stronger tidal distortion, the $\ell = 3$ component of the tidal distortion becomes more important, enabling coupling between modes differing by $\Delta\ell = 3$ and $\Delta\ell = 1$. In this case, the star and mode eigenfunctions will be asymmetric across the $x - y$ -plane, such that pulsations can be strongly trapped on either side of the star (i.e., the side facing toward or away from the companion). This leads to the observed ‘‘tidal trapping’’ or ‘‘single-sided pulsator’’ phenomenon (e.g., Handler et al. 2020; Kurtz et al. 2020).

In general, tidal coupling could lead to complex behavior of tidally perturbed pulsations, and the effects of strong tidal distortion, centrifugal, and Coriolis forces should all be taken into account. However, the simple case shown above demonstrates a straightforward mechanism through which tidal coupling could induce pulsations to naturally align with the x , y , and z -axes of the star. More thorough calculations incorporating the effects listed above, and using larger networks of coupled modes, will be needed for a full understanding of pulsations of tidally distorted stars.

9 SUMMARY, CONCLUSIONS, AND FUTURE DIRECTIONS

In this work, we report the discovery and analysis of a tight eclipsing binary with at least nine tidally tilted pulsation modes, TIC 184743498.

Evidence from our own ETV curve, as well as from Gaia’s discovery of an astrometric acceleration solution, both indicate that there is a third star in the system in a wide orbit of thousands of days. We have analysed the available archival data for this system to investigate the stellar parameters and the evolutionary state of the system using an SED fitting code. This code incorporates measured RVs from Gaia, stellar evolution models, and other parameters extracted from the light curve with the modeling code LIGHTCURVEFACTORY. We find that the pulsating primary star has $M_1 \simeq 1.83 M_\odot$, $R_1 \simeq 1.72 R_\odot$, and $T_{\text{eff},1} \simeq 8500$ K, while the secondary has $M_2 \simeq 1.37 M_\odot$, $R_2 \simeq 1.35 R_\odot$, and $T_{\text{eff},2} \simeq 6870$ K. The primary star has evolved somewhat away from the ZAMS at an age of 460 Myr, while the secondary star is still on the ZAMS. The uncertainties on the properties of the inferred third star are large, but it is likely not too different from the secondary star in the inner binary, and apparently contributes $\sim 10\%$ of the system light.

We then analyzed the pulsations of TIC 184743498 in detail. The system exhibits nine pulsation modes, 5 of which have pulsation amplitude maxima at the binary eclipses and phase shifts of π at the ELV peaks. We conclude that the first 5 pulsations can be explained by dipole modes Y_{10} about a pulsation axis which has been tilted into the orbital plane and which lies along the tidal axis. We call these ‘ $Y_{10,x}$ ’ modes.

Four other pulsations exhibit amplitude maxima at the ELV peaks and π phase shifts at the eclipses. We have shown that while the latter modes may appear to be Y_{11} modes based on their amplitudes and phases, this explanation is untenable because at the relatively low orbital inclination angle of this system (65°), such doublets would have an unmistakable central peak in their echelle diagram. Such a central peak is a visual description that the mode amplitude is nonzero at t_0 (i.e., at the eclipses) for these modes; however, the observed mode amplitudes do, in fact, vanish at the eclipses. The lack of such a central peak shows that these modes are actually Y_{10} about an axis we define as y , which is orthogonal to the tidal axis and the angular momentum axis. We term these ‘ $Y_{10,y}$ ’ modes.

We further found that one or both of two remaining singlet pulsation modes are also Y_{10} modes, but about the angular momentum axis z , and we investigated this hypothesis with single-star pulsation models. We found that the expected pulsation spectrum of radial modes with a star of the parameters derived from the SED fit is significantly less dense than the observed pulsation frequencies. Thus, the singlet pulsation modes cannot both be radial pulsations, but rather at least one of them must be a $Y_{10,z}$ mode, i.e., about the z -axis.

To study this hypothesis of three different pulsation axes, we explored a natural explanation in which strong tidal coupling can convert an otherwise uncoupled triplet of $\ell = 1$ dipole states to all Y_{10} modes, but about three orthogonal axes. These axes are (i) the tidal axis, (ii) the orbital angular momentum (i.e., stellar rotation) axis, and (iii) the direction in the orbital plane perpendicular to the tidal axis. This is exactly what we are seeing in the total set of 9 dipole modes and two singlet modes observed in TIC 184743498. Additionally, we show that the transformed original $Y_{1\pm 1}$ modes,

608 which have circulating pulsation modulations, are reduced to stand-
609 ing waves.

610 Every newly discovered tidally tilted pulsator presents dis-
611 tinctly unique behavior in its pulsations, and challenges previously
612 understood ideas about tidally tilted pulsations. TIC 184743498
613 contributes to this diversity as the first identified tri-axial pulsator.
614

615 More generally, the discovery reported here of a tri-axial set of
616 pulsation axes has a wider application to the broad subject of stel-
617 lar pulsations. We have seen that simple modes (such as doublet-
618 dipoles) are easier to understand in the context of tidal tilting than
619 complex multi-element modes; the latter of which are, in contrast,
620 far easier to spot in echelle diagrams. Finding the numerous dou-
621 blets in TIC 184743498, and their interpretation, have allowed us
622 to identify and interpret the modes of nearly all the prominent pul-
623 sations in this star.

624 With this in mind, we hope to search for more TTP candidate
625 stars with simpler modes such as doublets rather than those with
626 complex multi-element modes, such as HD 265435 (Jayaraman
627 et al. 2022). Future observations of TTPs in different photomet-
628 ric bands may reveal new insights into mode cavities/propagation
629 at different stellar layers, which, in turn, can provide an exquisite
630 new view into stellar interiors. We also highlight the fact that toy
631 models such as the one presented in this work should allow us to
632 develop a preliminary understanding of previously-unexplainable
633 phenomena, such as complicated mode couplings in stellar inter-
634 iors.

635 In this work we have also shown that, in systems with tidally
636 tilted modes, part of the pulsation geometry can be constrained, in
637 some cases rather tightly, by the determination of the orbital and
638 system parameters, especially the orbital inclination angle. It was
639 just this tilt of the orbit that allowed us to realize that we were deal-
640 ing with tri-axial pulsations in TIC 184743498, otherwise, the pul-
641 sational multiplet structures would be different. This orbital con-
642 straint can, and should, be applied to other TTP systems.

643 This work also motivates us to reexamine other previously
644 identified TTP candidates to see if any of their multiplets can be
645 fit into this paradigm of tidally induced doublets. In this regard,
646 the simple model for tidal tilting presented here needs expansion to
647 quadrupole modes. Once the signatures of tidally tilted quadrupole
648 modes, under the paradigm developed in this work, are understood,
649 we will be able to search for these specific features in other pul-
650 sating stars in binaries. Given a small set of stars with precisely
651 measured stellar parameters, and nearly complete sets of identified
652 pulsation modes, detailed stellar modeling of these modes will be
653 warranted.

654 Finally, we note that the 200-second cadence data that will
655 continue to come from *TESS*'s all-sky survey will be invaluable in
656 helping us determine the relationship between the stellar pulsation
657 axes and the strength of the tidal perturbation. These data will also
658 allow us to find all manner of new types of pulsations, and perhaps
659 answer some of the lingering questions in the field.

659 ACKNOWLEDGEMENTS

660 This paper includes data collected by the *TESS* mission. Fund-
661 ing for the *TESS* mission is provided by the NASA Science Mis-
662 sion directorate. Resources supporting this work were provided
663 by the NASA High-End Computing (HEC) Program through the
664 NASA Advanced Supercomputing (NAS) Division at Ames Re-
665 search Center to produce the SPOC data products. Some of the
666 data presented in this paper were obtained from the Mikulski

667 Archive for Space Telescopes (MAST). STScI is operated by the
668 Association of Universities for Research in Astronomy, Inc., un-
669 der NASA contract NAS5-26555. Support for MAST for non-HST
670 data is provided by the NASA Office of Space Science via grant
671 NNX09AF08G and by other grants and contracts.

672 G. H. acknowledges financial support from the Polish National
673 Science Center (NCN), grant no. 2021/43/B/ST9/02972. This re-
674 search was supported by the Erasmus+ programme of the European
675 Union under grant number 2017-1-CZ01-KA203-035562.

676 T. B. has received funding for this project from the HUN-REN
677 Hungarian Research Network.

678 Data availability

679 The *TESS* data used in this paper are available on MAST. All other
680 data used are reported in tables within the paper. The *MESA* binary
681 evolution 'inlists' are available on the *MESA* Marketplace: [http://](http://cococubed.asu.edu/mesa_market/inlists.html)
682 cococubed.asu.edu/mesa_market/inlists.html.

683 REFERENCES

- 684 Aerts C., Christensen-Dalsgaard J., Kurtz D. W., 2010, *Astero-*
685 *seismology*
686 Asplund M., Grevesse N., Sauval A. J., Allende Prieto C., Kisel-
687 man D., 2004, *A&A*, 417, 751
688 Baglin A., Breger M., Chevalier C., Hauck B., Le Contel J. M.,
689 Sareyan J. P., Valtier J. C., 1973, *A&A*, 23, 221
690 Blomme R. et al., 2023, *A&A*, 674, A7
691 Borkovits T. et al., 2019, *MNRAS*, 483, 1934
692 Borkovits T., Rappaport S. A., Hajdu T., Maxted P. F. L., Pál A.,
693 Forgács-Dajka E., Klagyivik P., Mitnyan T., 2020, *MNRAS*, 493,
694 5005
695 Breger M., 1979, *PASP*, 91, 5
696 —, 2000, in *Astronomical Society of the Pacific Conference Se-*
697 *ries*, Vol. 210, *Delta Scuti and Related Stars*, Breger M., Mont-
698 gomery M., eds., p. 3
699 Campbell W. W., Wright W. H., 1900, *ApJ*, 12, 254
700 Castelli F., Kurucz R. L., 2003, in *IAU Symposium*, Vol. 210,
701 *Modelling of Stellar Atmospheres*, Piskunov N., Weiss W. W.,
702 Gray D. F., eds., p. A20
703 Choi J., Dotter A., Conroy C., Cantiello M., Paxton B., Johnson
704 B. D., 2016, *ApJ*, 823, 102
705 Colacevich A., 1935, *PASP*, 47, 231
706 Cutri R. M., et al., 2013, *VizieR Online Data Catalog*, II/328
707 Dotter A., 2016, *ApJS*, 222, 8
708 Eddington A. S., 1926, *The Internal Constitution of the Stars*
709 Fath E. A., 1935, *PASP*, 47, 232
710 Ford E. B., 2005, *AJ*, 129, 1706
711 Fuller J., Kurtz D. W., Handler G., Rappaport S., 2020, *MNRAS*
712 Gaia Collaboration et al., 2023, *A&A*, 674, A1
713 Halbwachs J.-L. et al., 2023, *A&A*, 674, A9
714 Handler G. et al., 2020, *Nature Astronomy*
715 Holdsworth D. L. et al., 2021, *MNRAS*, 506, 1073
716 Jayaraman R., Handler G., Rappaport S. A., Fuller J., Kurtz D. W.,
717 Charpinet S., Ricker G. R., 2022, *ApJ*, 928, L14
718 Jenkins J. M. et al., 2016, in *Society of Photo-Optical Instrumen-*
719 *tation Engineers (SPIE) Conference Series*, Vol. 9913, *Software*
720 *and Cyberinfrastructure for Astronomy IV*, Chiozzi G., Guzman
721 J. C., eds., p. 99133E
722 Johnston C., Tkachenko A., Van Reeth T., Bowman D. M.,
723 Pavlovski K., Sana H., Sekaran S., 2023, *A&A*, 670, A167

- 724 Katz D. et al., 2023, *A&A*, 674, A5
725 Kochanek C. S. et al., 2017, *PASP*, 129, 104502
726 Kovács G., Zucker S., Mazeh T., 2002, *A&A*, 391, 369
727 Kristiansen M. H. K. et al., 2022, *PASP*, 134, 074401
728 Kurtz D. W., 1982, *MNRAS*, 200, 807
729 —, 2022, *ARA&A*, 60, 31
730 Kurtz D. W. et al., 2011, *MNRAS*, 414, 2550
731 —, 2020, *MNRAS*, 494, 5118
732 Kurtz D. W., Holdsworth D. L., 2020, in *Astrophysics and Space*
733 *Science Proceedings*, Vol. 57, *Dynamics of the Sun and Stars;*
734 *Honoring the Life and Work of Michael J. Thompson*, Monteiro
735 M. J. P. F. G., García R. A., Christensen-Dalsgaard J., McIntosh
736 S. W., eds., pp. 313–319
737 Lightkurve Collaboration et al., 2018, *Lightkurve: Kepler and*
738 *TESS time series analysis in Python. Astrophysics Source Code*
739 *Library*
740 Murphy S. J., Hey D., Van Reeth T., Bedding T. R., 2019, *MN-*
741 *RAS*, 485, 2380
742 Ochsenbein F., Bauer P., Marcout J., 2000, *A&AS*, 143, 23
743 Pamyatnykh A. A., Dziembowski W. A., Handler G., Pikall H.,
744 1998, *A&A*, 333, 141
745 Paxton B., Bildsten L., Dotter A., Herwig F., Lesaffre P., Timmes
746 F., 2011, *ApJS*, 192, 3
747 Paxton B. et al., 2015, *ApJS*, 220, 15
748 —, 2019, *ApJS*, 243, 10
749 Rappaport S. A. et al., 2022, *MNRAS*, 513, 4341
750 —, 2023, *MNRAS*, 521, 558
751 —, 2021, *MNRAS*, 503, 254
752 Reed M. D., Brondel B. J., Kawaler S. D., 2005, *ApJ*, 634, 602
753 Ricker G. R. et al., 2015, *Journal of Astronomical Telescopes,*
754 *Instruments, and Systems*, 1, 014003
755 Shappee B. J. et al., 2014, *ApJ*, 788, 48
756 Southworth J., Bowman D. M., Tkachenko A., Pavlovski K.,
757 2020, *MNRAS*, 497, L19
758 Stassun K. G. et al., 2019, *AJ*, 158, 138
759 Van Reeth T., Johnston C., Southworth J., Fuller J., Bowman
760 D. M., Poniatowski L., Van Beeck J., 2023, *A&A*, 671, A121